Les mutations du gène NONO sont responsables d'un nouveau syndrome de déficience intellectuelle lié au dysfonctionnement des synapses inhibitrices

Langouët, Maéva ; Mircsof, Dennis ; Rio, Marlène ; Amiel, Jeanne ; Brown, Steven A ; Colleaux, Laurence

DOI: https://doi.org/10.1051/medsci/20163206015

Other titles: Mutations in NONO lead to syndromic intellectual disability and inhibitory synaptic defects

nature neuroscience

ARTICLES

Mutations in *NONO* lead to syndromic intellectual disability and inhibitory synaptic defects

Dennis Mircsof[1,2,14], Maéva Langouët[3,14], Marlène Rio[3,4], Sébastien Moutton[3], Karine Siquier-Pernet[3], Christine Bole-Feysot[5], Nicolas Cagnard[6], Patrick Nitschke[6], Ludmila Gaspar[1], Matej Žnidarič[1], Olivier Alibeu[5], Ann-Kristina Fritz[7], David P Wolfer[7], Aileen Schröter[8], Giovanna Bosshard[2], Markus Rudin[8], Christina Koester[2], Florence Crestani[2], Petra Seebeck[9], Nathalie Boddaert[3,10], Katrina Prescott[11], The DDD Study[12], Rochelle Hines[13], Steven J Moss[13], Jean-Marc Fritschy[2], Arnold Munnich[3], Jeanne Amiel[3,4], Steven A Brown[1,15], Shiva K Tyagarajan[2,15] & Laurence Colleaux[3,15]

The NONO protein has been characterized as an important transcriptional regulator in diverse cellular contexts. Here we show that loss of NONO function is a likely cause of human intellectual disability and that NONO-deficient mice have cognitive and affective deficits. Correspondingly, we find specific defects at inhibitory synapses, where NONO regulates synaptic transcription and gephyrin scaffold structure. Our data identify *NONO* as a possible neurodevelopmental disease gene and highlight the key role of the DBHS protein family in functional organization of GABAergic synapses.

NONO, the non-octamer-containing, POU-domain DNA-binding protein, also known as p54NRB, belongs to the highly conserved *Drosophila* behavior/human splicing (DBHS) protein family. This family includes three members in mammals: NONO, paraspeckle component 1 (PSPC1) and splicing factor proline/glutamine-rich (SFPQ, also known as PSF). DBHS proteins are nuclear proteins forming homo- and heterodimers *in vivo*[1,2], and previous literature documents their involvement in various aspects of RNA metabolism[3]. Studies *in vitro* suggest that they act in transcriptional activation and repression[4–6], splicing[7,8], pre-mRNA processing[9] and RNA transport[10,11]. In addition, they are major components of nuclear paraspeckles, which have been recognized as nuclear RNA-holding structures for edited RNAs[12,13] that likely function in stress-mediated regulation via nuclear retention of transcripts[14–16]. NONO and other DBHS family members also serve as transcriptional cofactors for correct circadian clock function in both flies and mammals, where they regulate the circadian clock via interaction with PER proteins[17–20]. However, no study so far has linked impaired function of these proteins to human disease. Here we demonstrate that the NONO protein extensively regulates synaptic transcript abundance and that its mutation or deletion results in impaired cognitive function in both humans and mice.

Human intellectual disability is characterized by limitations in intellectual functioning and adaptive behavior. Recent developments in next-generation sequencing and whole-exome sequencing have empowered detection of disease variants in intellectual disability[21–23]. Through these strategies, many new genes have been identified. By contrast, identifying the underlying pathophysiological mechanisms has remained a considerable challenge. Besides the molecular characterization of a novel clinically recognizable intellectual disability condition, our study has been empowered by the analysis of NONO-deficient mice, which share both transcriptional and morphological characteristics with patients. Our data suggest that NONO may contribute to the regulation of RNA metabolism underlying local regulation of dendritic spine morphology and that it has a major and unsuspected role in regulating synaptic morphology at a cellular level.

RESULTS

Mutations in human *NONO* are a likely cause of intellectual disability

Whole-exome sequencing was carried out in parallel in two unrelated male intellectual disability patients (MCCID1 and MCCID2), who presented the same gestalt of slender build, macrocephaly, distinctive facial features, shy behavior, a thick corpus callosum and a small cerebellum

[1]Chronobiology and Sleep Research Group, Institute of Pharmacology and Toxicology, University of Zürich, Zürich, Switzerland. [2]Neuromorphology Group, Institute of Pharmacology and Toxicology, University of Zürich, Zürich, Switzerland. [3]INSERM UMR 1163, Laboratory of Molecular and Pathophysiological Bases of Cognitive Disorders, Paris Descartes–Sorbonne Paris Cité University, Imagine Institute, Necker-Enfants Malades Hospital, Paris, France. [4]Service de Génétique, Hôpital Necker-Enfants Malades, Assistance Publique Hôpitaux de Paris, Paris, France. [5]Genomic Platform, INSERM UMR 1163, Paris Descartes–Sorbonne Paris Cité University, Imagine Institute, Necker-Enfants Malades Hospital, Paris, France. [6]Bioinformatic Platform, INSERM UMR 1163, Paris Descartes–Sorbonne Paris Cité University, Imagine Institute, Necker-Enfants Malades Hospital, Paris, France. [7]Institute of Anatomy, University of Zürich and Institute of Human Movement Sciences and Sport, ETH Zürich, Switzerland. [8]Molecular Imaging and Functional Pharmacology Group, University of Zürich, Zürich, Switzerland. [9]Center for Integrative Rodent Physiology, University of Zürich, Zürich, Switzerland. [10]Service de radiologie pédiatrique, Hôpital Necker-Enfants Malades, Assistance Publique Hôpitaux de Paris, Paris, France. [11]Yorkshire Regional Genetics Service, Leeds Teaching Hospitals National Health Service Trust, Department of Clinical Genetics, Chapel Allerton Hospital, Chapeltown Road, Leeds, UK. [12]A full list of consortium members appears in the **Supplementary Note**. [13]Tufts University, Sackler School of Graduate Biomedical Sciences, Boston, Massachusetts, USA. [14]These authors contributed equally to this work. [15]These authors jointly directed this work. Correspondence should be addressed to L.C. (laurence.colleaux@inserm.fr), S.K.T. (tyagarajan@pharma.uzh.ch) or S.A.B. (steven.brown@pharma.uzh.ch).

Received 30 July; accepted 15 October; published online 16 November 2015; doi:10.1038/nn.4169

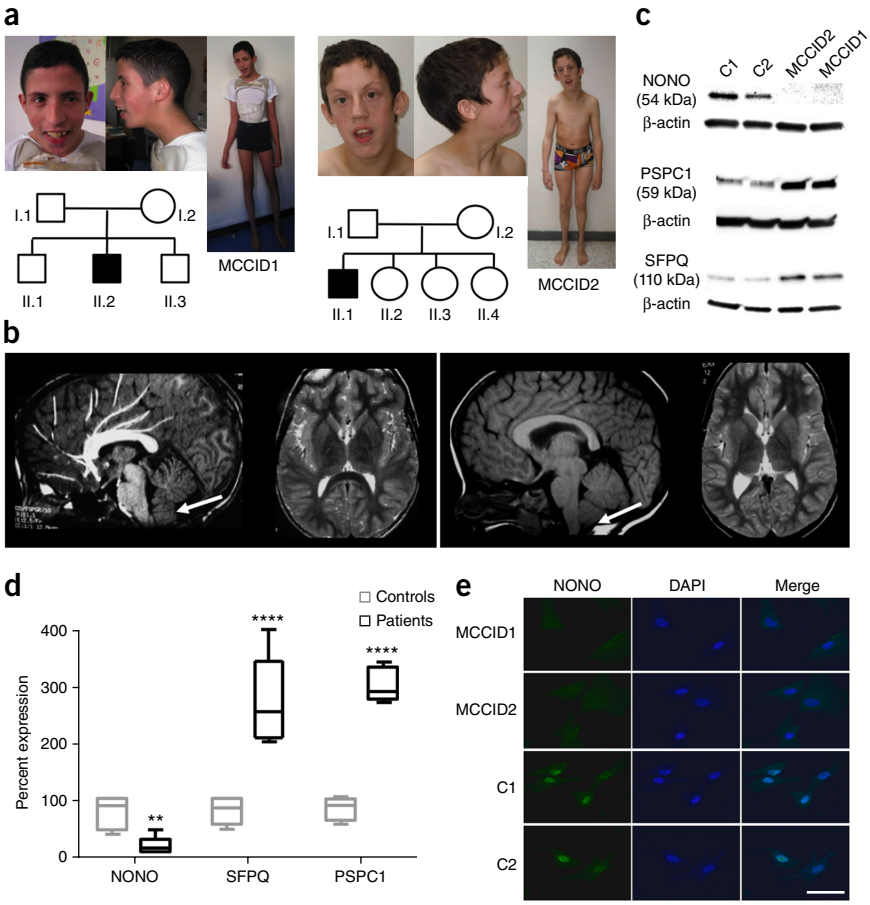

Figure 1 *NONO* mutations and their functional consequences. (**a**) Photographs and pedigree of both patients. Filled symbols indicate the affected individuals. (**b**) Sagittal T1 and axial FSE T2 brain MRI of patient MCCID1 at 9 years old (left) and MCCID2 at 8 years old (right) showing a thick corpus callosum, small cerebellum and Chiari I malformation (arrows). (**c**) Immunoblots showing an absence of the NONO protein and overexpression of PSPC1 and SFPQ proteins in patients' cells compared to controls (C1 and C2). (**d**) Quantification of DBHS protein levels relative to the amount of total proteins, expressed as percentage of control values. Box plot derived from two independent experiments with two technical replicates; whiskers show minimum and maximum values; center line represents median; and box limits represent interquartile range. Significance was calculated using two-way analysis of variance (ANOVA) test with Sidak correction and $P = 0.008268$ for NONO, 0 for SFPQ and 0 for PSPC1. Here and in subsequent figures, $*P < 0.05$, $**P < 0.01$, $***P < 0.001$, $****P < 0.0001$. (**e**) Immunofluorescence showing the absence of the NONO protein in patients' cells and presence in controls. Scale bar represents 50 μm.

(**Fig. 1a**,**b** and **Supplementary Table 1** and Online Methods). Supposing that the same disease gene was shared by the two patients, only the X-linked *NONO* gene emerged as a candidate (**Supplementary Table 2**). Capillary sequencing confirmed the *de novo* occurrence of a splice site variant affecting the last base of exon 10 in patient MCCID1 (NM_001145408.1:c.1131G>A; Ala377Ala) (**Supplementary Fig. 1**). The variant identified in patient MCCID2 was a one-base-pair insertion in the last coding exon (NM_001145408.1: c.1394dup; Asn466Lysfs*13) inherited from his healthy mother (**Supplementary Fig. 1**). The role of *NONO* mutations in the etiology of intellectual disability was further supported by the identification of a third patient from a separate cohort, in the Deciphering Developmental Disorders (DDD) study[24]. This patient carried a nonsense mutation in exon 10 (NM_001145408.1:c.1093C>T; p.Arg365*) and had similar morphological and behavioral characteristics to the other two patients (**Supplementary Fig. 2** and **Supplementary Table 1**).

Immunoblot analyses of cultured skin fibroblast lysates using an anti-NONO polyclonal antibody showed little or no NONO protein in MCCID1 and MCCID2 patient cells, unlike in controls (**Fig. 1c**,**d**). These results were confirmed by immunocytochemistry using the same antibody (**Fig. 1e**), as well as by immunoblot with another polyclonal antibody (**Supplementary Fig. 3**).

Altered gene expression in cells from patients and *Nono^{gt}* mice

Microarray analysis of cultured skin fibroblast RNAs in patients compared to controls revealed a marked modification in the global pattern of gene expression between the two groups. Indeed, hierarchical clustering analysis showed that the patient group formed an independent cluster away from the control RNAs (**Fig. 2a**). A total of 389 differentially expressed genes were shared by the two patients, with 372 transcripts being similarly affected (213 downregulated and 159 upregulated), whereas only 17 transcripts were deregulated in opposite directions (**Fig. 2b** and **Supplementary Table 3**). Notably, increased transcript levels of the other DBHS family members, *PSPC1* (2.22 and 2.78 fold respectively) and *SFPQ* (1.54- and 1.71-fold, respectively), were detected in both patients compared to controls. These expression data were confirmed by western blot analysis showing increased amounts of PSPC1 and SFPQ proteins in patient fibroblasts compared to controls (**Fig. 1c**,**d**).

To further characterize the physiological role of NONO, we analyzed a mouse model in which the *Nono* gene had been disrupted by gene trap (gt)[20]. Gene expression analysis in adult dermal fibroblasts from wild-type and *Nono^{gt}* mice revealed global transcriptional deregulation in the mutant mice compared to controls in patterns similar to those of human patients and controls. When human and mouse data sets were merged and submitted to a hierarchical clustering with the Spearman correlation similarity measure, the samples were split in two main groups. *Nono^{gt}* mice samples segregated with the patient group, whereas wild-type mouse samples segregated with the human control samples (**Fig. 2c**). Moreover, consistent with the role for the NONO protein in the circadian clock established in mouse fibroblasts and in mice themselves[20], cultured skin fibroblasts from patients showed a reduced amplitude of circadian oscillations (**Supplementary Fig. 4**). Taken together, these data demonstrated a regulatory role of NONO conserved through evolution and supported the relevance of the *Nono^{gt}* model for further elucidation of the disease mechanism in patients.

Phenotypic comparison of patients and *Nono^{gt}* mice

Visual inspection and CT scan revealed that *Nono^{gt}* mice displayed a flattened nose, mimicking the facial anomalies observed in the patients (**Fig. 3a–c** and **Supplementary Table 4**). Similarly, a smaller cerebellum was observed in mutant mice (**Fig. 3d**, **Supplementary Fig. 5** and **Supplementary Table 4**) and patients (**Fig. 1b** and **Supplementary Table 1**),

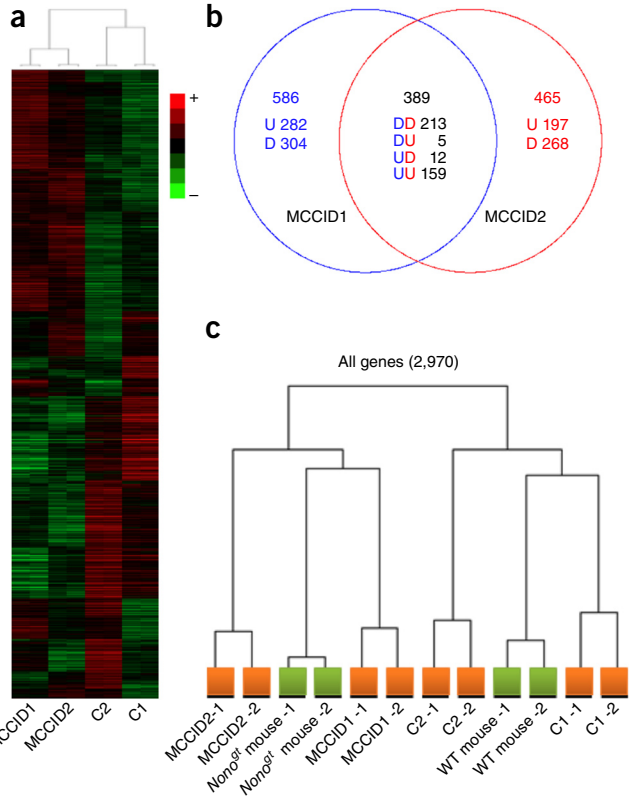

Figure 2 Transcriptome analysis in human and mouse cells. (**a**) Heat map cluster analyses indicating similarity in expression profile among probes from the two patients and differences compared to the two controls. High detection signals relative to the mean are red, low detection signals are green. The cut-off for inclusion in the heat map was a 1.5-fold alteration of probe expression for both patients. Color scale ranges between –0.5 (green) and 0.5 (red). (**b**) Venn diagram showing the number of genes expressed in common or differentially expressed in the two patients compared to the mean of the two controls. Significant differences are based on a 1.5-fold difference and $P < 0.05$. U, up; D, down. (**c**) Hierarchical clustering analysis of combined mouse and human orthologous genes, resulting in a separation highlighting similarity of mouse and human transcriptional dysregulation. WT, wild type. Human samples are shown in orange and mouse samples are shown in green.

as well as other structural anomalies (**Supplementary Tables 1** and **4**). Behaviorally, mice showed impaired performance in the Morris water maze, a test of spatial memory (**Fig. 3e,f**), as well as a marked anxiety phenotype documented via prepulse inhibition, and increased risk aversion in an open field and light-dark test (**Supplementary Fig. 6**).

NONO regulates the abundance of synaptic RNAs

Immunofluorescence analysis using anti-NONO antibodies detected strong immunoreactivity in mouse brain, including cortex and hippocampus (**Fig. 4a**). Staining was strongest in neuronal (NeuN-positive) nuclei in CA1 and CA3 pyramidal regions and granule cells of the dentate gyrus, but absent from neighboring astrocytes (GFAP-positive) (**Supplementary Fig. 7**). Gene expression analysis in hippocampi of wild-type and *Nono*^{gt} mice identified 882 differentially expressed genes (**Fig. 4b**) (GEO accession code GSE62571), including the two other DBHS family members, *Sfpq* and *Pspc1*, that were upregulated in NONO-deficient patient fibroblasts (**Supplementary Fig. 8**). Protein levels of these orthologs were also upregulated in *Nono*^{gt} hippocampi (**Supplementary Fig. 9**). Notably, mRNA levels of *Gabra2*, the $GABA_A$ receptor ($GABA_AR$) α2 subunit, were markedly reduced in hippocampi of *Nono*^{gt} mice compared to controls, a result confirmed by quantitative real-time PCR and western blot analyses (**Supplementary Figs. 8**, **10** and **11**). Moreover, pathway analyses suggested that NONO-regulated genes were markedly enriched in Gene Ontology categories related to synaptic functions (**Supplementary Table 5**).

To support this *in silico* prediction, we compared the synaptosomal transcriptomes from *Nono*^{gt} and control mice. RNA was extracted from synaptosomal fractions obtained by density gradient ultracentrifugation[24]. The quality of this fractionation was confirmed by verifying enrichment of known synaptically transported RNAs and depletion of known nuclear RNAs relative to the whole transcriptome (**Supplementary Fig. 10a–c**) (GEO accession code GSE62573). We found that 30.5% of NONO-regulated transcripts were in fact synaptosomal, including *Gabra2* (**Supplementary Fig. 10d**). This represents a significant over-representation compared to whole transcriptome (**Supplementary Table 6**, $P = 0.0007$; **Supplementary Table 7**). Hence,

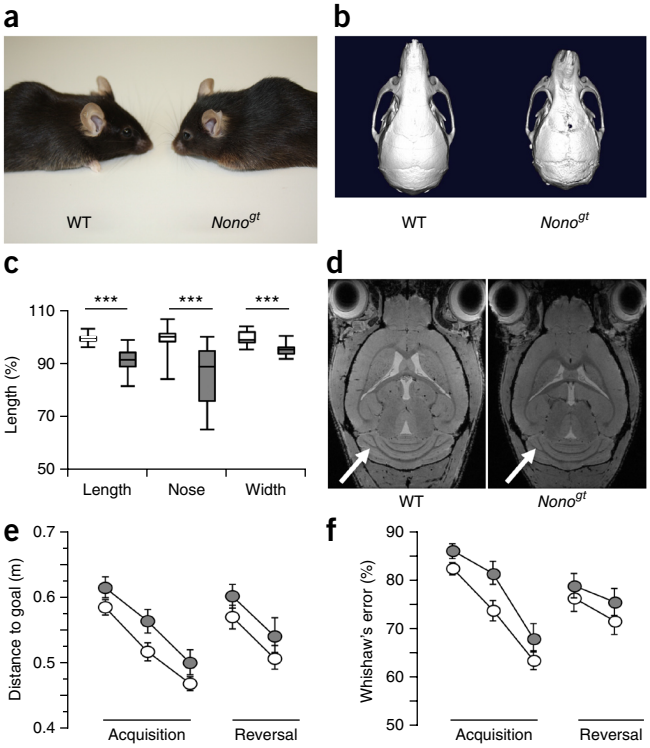

Figure 3 Functional consequences of NONO deficiency in mice. (**a**) Side view of representative *Nono*^{gt} mouse (right) compared to wild-type littermate (WT, left). (**b**) CT scan analysis indicating a flattened and distorted nose in *Nono*^{gt} mice (right) compared to WT (left). (**c**) Box-and-whisker quantification of skull length, width and nose length in *Nono*^{gt} mice (gray) compared to wild-type littermate (white) (center, meridian; box limit, quartiles 1 and 3; whiskers, minimum and maximum). $n = 20$ mice per genotype. $^{***}P < 0.001$; Student's *t*-test. (**d**) MRI scan of representative *Nono*^{gt} mouse (right) compared to wild-type littermate (left). Arrows indicate cerebellum. Also see **Supplementary Figure 5** and **Supplementary Table 4**. (**e**,**f**) Behavior of *Nono*^{gt} mice and WT littermates in Morris water maze, $n = 16–20$ per genotype. Gray, *Nono*^{gt}; white, WT. Bars represent means ± s.e.m. (**e**) Gallagher's proximity test scores (average distance of mice from goal as fraction of total distance). Repeated ANOVA, gene $P < 0.0237$, time $P < 0.001$, interaction $P = 0.9869$. (**f**) Whishaw's error (percentage of path outside an 18-cm-wide corridor connecting release point and goal). Gene $P < 0.0215$, time $P < 0.001$, interaction $P = 0.7927$.

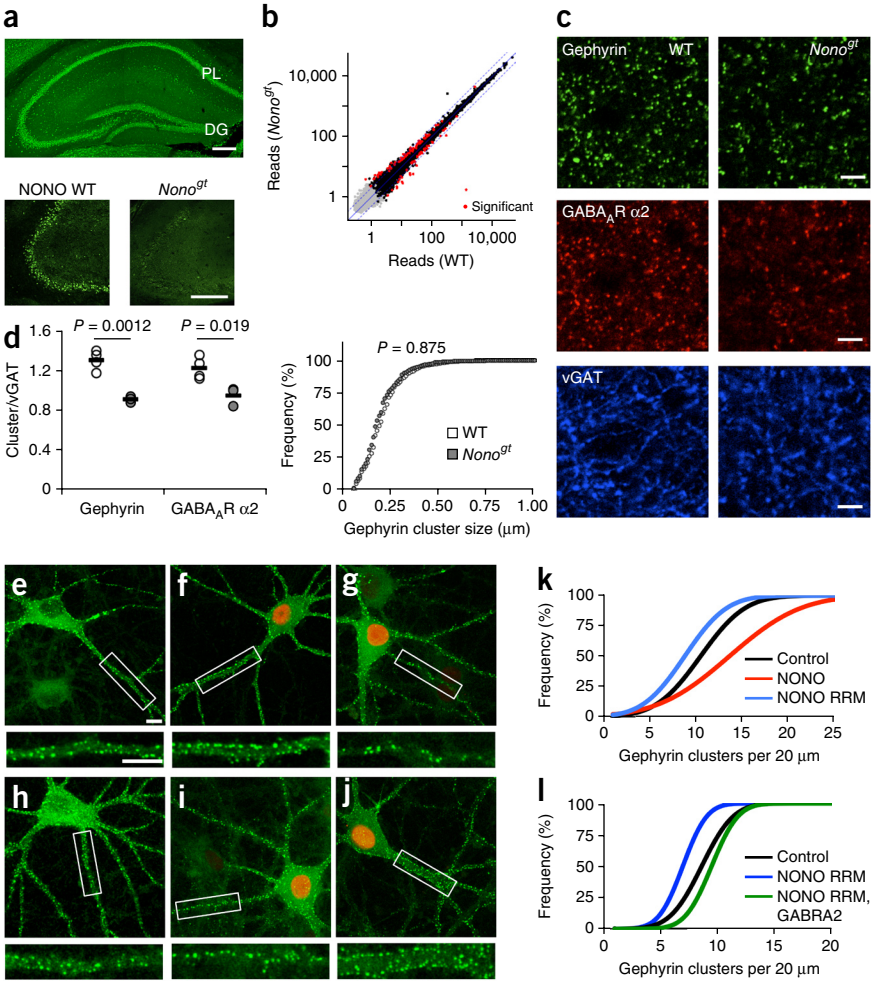

Figure 4 Effects of NONO deficiency on synaptic biology. (**a**) Immunofluorescence labeling of NONO in wild-type (WT; top) and *Nono*^{gt} (bottom) mouse coronal brain sections. PL, pyramidal cell layer; DG, dentate gyrus. Scale bars, 250 μm. (**b**) Scatter plot of hippocampal transcriptome from WT and *Nono*^{gt} mice. Red, differentially expressed genes, $P \leq 0.01$ and log ratio ≥ 0.5. Blue lines indicate twofold difference. (**c**) Immunohistochemical staining for inhibitory postsynaptic marker gephyrin (green), $GABA_AR$ α2 receptor (red) and the presynaptic marker vGAT (blue) in WT and *Nono*^{gt} mice in the CA3 stratum radiatum of the hippocampus. Scale bars, 5 μm. (**d**) Left, scatter plot quantification of gephyrin and GABAR α2 relative to VGAT density. Right, frequency distribution of gephyrin cluster size. White circles, WT; black circles, *Nono*^{gt}. (**e**–**l**) Immunofluorescence analysis of gephyrin postsynaptic clusters *in vitro*. (**e**–**g**) Primary hippocampal rat neurons expressing control GFP-gephyrin alone (**e**), coexpressed with myc-NONO (**f**) or coexpressed with RNA binding-deficient myc-NONO-RRM (**g**). Boxed region is magnified beneath. (**h**–**j**) Primary hippocampal rat neurons expressing control GFP-gephyrin alone (**h**), coexpressed with myc-NONO-RRM (**i**) or coexpressed with myc-NONO-RRM and $GABA_AR$ α2 (**j**). Scale bars, 10 μm. (**k**) Quantification of gephyrin cluster density in **e**–**g** by normal density distribution modeling, in 9 neurons from each of 3 independent experiments. Control × NONO $P = 0.001$, control × myc-NONO-RRM $P = 0.009$ using Kolmogorov-Smirnov test. (**l**) Identical curve-fit quantification of gephyrin clusters in **h**–**j**, showing complete rescue of the impaired gephyrin cluster distribution by $GABA_AR$ α2 overexpression. Control × NONO-RRM $P = 0.009$, control × NONO-RRM + $GABA_AR$ α2 $P = 0.563$, NONO-RRM × NONO-RRM + $GABA_AR$ α2 $P = 0.014$ using Kolmogorov-Smirnov test.

our data show that NONO plays a specific and important role in the regulation of synaptic RNAs.

Inhibitory synaptic structural defects in *Nono*^{gt} mice

Gabra2 encodes a subunit of the $GABA_ARs$ that potentiate most fast synaptic inhibition in the brain. Previous studies have demonstrated that $GABA_ARs$ are anchored postsynaptically by gephyrin, which self-assembles into a scaffold and interacts with the cytoskeleton. The binding of gephyrin to $GABA_ARs$ is mediated by interaction sites in the intracellular loop of $GABA_AR$ α1, α2 and α3 subunits[25]. We thus tested the consequences of loss of NONO at inhibitory synapses by immunohistological studies of brain sections from wild-type and *Nono*^{gt} mice, using antibodies directed against $GABA_AR$ α2 and gephyrin. Postsynaptic punctate staining for gephyrin and $GABA_AR$ α2 was significantly reduced in the CA3 hippocampal region of *Nono*^{gt} mice ($P = 0.0012$), while staining of the presynaptic vesicular GABA transporter marker (vGAT) was unaffected (**Fig. 4c**). Quantitative evaluations showed that the number of gephyrin clusters was significantly reduced, but average cluster size was conserved (**Fig. 4d**). Western blot analyses showed markedly reduced $GABA_AR$ α2 levels in total brain lysates and synaptosomes (**Supplementary Figs. 10** and **11**). By contrast, gephyrin levels were similar in wild type and *Nono*^{gt} in all compartments analyzed (**Supplementary Fig. 11**). Taken together, these data suggest that reduced $GABA_AR$ α2 levels in *Nono*^{gt} mice are likely to be due to transcriptional deregulation. In turn, altered gephyrin clustering is likely to be a downstream consequence of altered synaptic composition because of these transcriptional changes.

Synaptic defects in *Nono*^{gt} mice probably have a cellular origin

In principle, the anomalies observed in *Nono*^{gt} mice could arise from either cellular synaptic defects or broader neurodevelopmental changes. To distinguish between these possibilities and uncover potential cell-autonomous phenotypes, we used high-resolution fluorescence *in situ* hybridization to analyze dissociated hippocampal neurons from wild-type and *Nono*^{gt} mice. As in intact brain slices, we observed a significant reduction of *Gabra2* transcripts in NONO-deficient neurons ($P = 0.0020$), but unchanged transcript levels for the other postsynaptic markers collybistin (*Arhgef9*) and *Gabra1* (**Supplementary Fig. 12**). At the protein level, these cultures showed the same reduction of gephyrin scaffolding puncta and $GABA_AR$ α2 levels (**Fig. 4**), demonstrating that primary culture neurons from these mice recapitulated the key cytological features observed in *Nono*^{gt} mouse hippocampi. We therefore used this cellular model for functional analysis of NONO in postsynaptic biology.

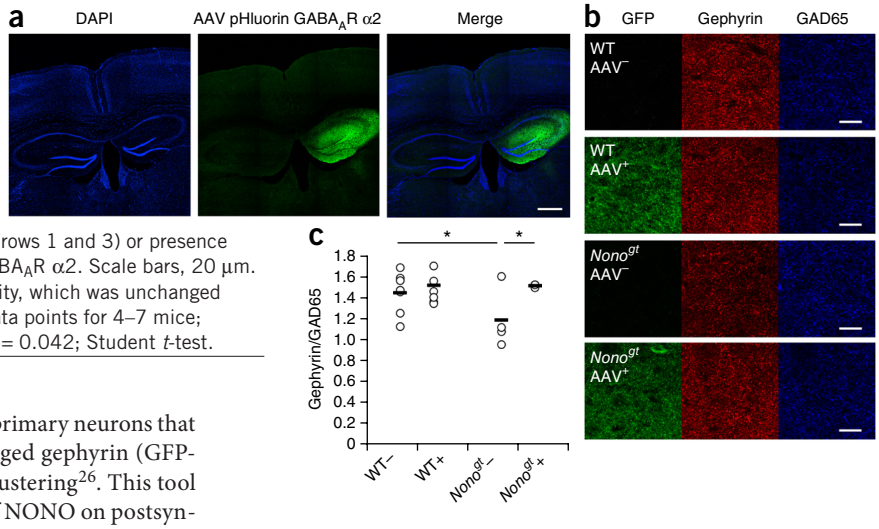

Figure 5 GABA receptor overexpression rescues synaptic structural defects. (**a**) Fluorescence microscopy of hippocampal slices after unilateral stereotactic injection of AAV expressing pHluorin-tagged GABA$_A$R α2. Scale bar, 500 µm. (**b**) Immunohistochemical staining for GFP (green, left), gephyrin (red, middle) and the presynaptic marker GAD65 (blue) in wild-type (rows 1 and 2) and *Nono^{gt}* mice (rows 3 and 4) in the stratum radiatum of CA3 in the hippocampus in the absence (rows 1 and 3) or presence (rows 2 and 4) of AAV expressing pHluorin-tagged GABA$_A$R α2. Scale bars, 20 µm. (**c**) Quantification of gephyrin relative to GAD65 density, which was unchanged across experimental conditions. Scatter plot shows data points for 4–7 mice; WT × *Nono^{gt}* AAV–, $P = 0.013$; WT × *Nono^{gt}* AAV+, $P = 0.042$; Student *t*-test.

It has been previously established in cultured primary neurons that overexpression of green fluorescent protein-tagged gephyrin (GFP-gephyrin) has no apparent effect on gephyrin clustering[26]. This tool was used to examine in more detail the effects of NONO on postsynaptic structures. Conversely to what was observed in NONO-deficient mouse neurons, overexpression of myc-tagged NONO in wild-type primary hippocampal neurons expressing GFP-gephyrin caused a significant increase in density of GFP-gephyrin puncta compared to that in neurons transfected with GFP-gephyrin alone ($P = 0.001$). By contrast, a reduction in GFP-gephyrin density was observed in cells transfected with a construct overexpressing a mutant form of the NONO protein, myc-NONO RRM (**Fig. 4e**,**f**). This construct contains four point mutations in the RNA recognition motif (RRM) and is therefore unable to bind to single-stranded RNAs. Thus, we conclude that the function of NONO in synaptic biology depends upon the RNA-binding domain of this protein.

Rescue by re-expression of GABA$_A$Rs at *Nono^{gt}* synapses

Gephyrin depends on the presence of GABA$_A$Rs to form postsynaptic clusters in GABAergic synapses, and the size and density of gephyrin scaffolding can be correlated to strength and frequency of GABAergic transmission[25,26]. Gephyrin clustering is largely impaired in the mice lacking the GABA$_A$R α2 subunit (*Gabra2$^{-/-}$*)[27]. Therefore, we hypothesized that the altered gephyrin distribution observed in NONO-deficient neurons might in part be the consequence of *Gabra2* transcript deregulation.

If this hypothesis were true, then we might expect the morphological defects observed in *Nono^{gt}* neurons to be rescued by overexpressing GABA$_A$R α2. And indeed, transfection of plasmids expressing GABA$_A$R α2 was able to rescue the reduced gephyrin cluster density observed in cultured neurons transfected with myc-NONO-RRM (**Fig. 4g**,**h**). Similarly, unilateral viral infection of hippocampal neurons with adeno-associated viruses overexpressing GABA$_A$R α2 *in vivo*[28] was also able to rescue the reduced cluster density in the infected hippocampus, while the contralateral uninfected side remains unaffected (**Fig. 5**). Both these observations support the view that alteration of GABA$_A$R α2 levels is key to the etiology of the morphological defects observed in *Nono^{gt}* neurons.

DISCUSSION

In this study, we have shown that *NONO* null mutations are the likely cause of a clinically recognizable intellectual disability syndrome. One of the three patients that we identified also harbors a deletion at 15q13.3, a locus at which copy number variation predisposes to epilepsy and intellectual disability[29]. While we cannot exclude a minor effect of the 15q13.3 deletion on the neurological presentation of patient MCCID1, its absence in the other two NONO-deficient patients argues that *NONO* null mutations result in the syndromic intellectual disability we document.

A mouse model deficient in NONO recapitulated the main features of this syndrome. Studying brains and neurons from these mutant mice suggested that NONO has an unsuspected function in regulating inhibitory synaptic biology, results also consistent with intellectual and anxiety phenotypes of these mice. Previous studies have identified NONO as a member of a neuronal RNA transport complex[10] and demonstrated increased NONO abundance at synapses in response to synaptic activity[30], but no study to our knowledge has yet linked dysfunction in NONO or other DBHS proteins to any human disease. Our studies clearly demonstrate that, in the brain, NONO actively regulates expression of synaptic transcripts on a global scale: one-third of all NONO-regulated transcripts are synaptic. These data point to an essential role of NONO in neuronal connectivity and raise the issue of the function of the two other DBHS proteins in this process.

Based upon such widespread regulation, the phenotypes observed in patients and mice are likely the collective result of many factors arising from NONO-mediated transcriptional defects. For example, we have previously shown that NONO is important to circadian clock control[17], and circadian clock defects are observed in NONO-deficient mice[20], as well as in patient and mouse fibroblasts. Various studies have shown that altering the circadian system affects learning and memory[31], so local clock function may contribute to the phenotype observed in NONO-deficient neurons. Gene ontological enrichment suggested that many further aspects of synaptic function might also be affected.

Our morphological studies demonstrate that this defect in the regulation of synaptic RNA metabolism ultimately regulates even dendritic spine morphology, as visualized by the scaffolding protein gephyrin. These defects in gephyrin scaffolding are mirrored by changes in the receptors that anchor it. The most abundant hippocampal GABA$_A$R isoform, GABA$_A$R α2, was downregulated in NONO-deficient cells and mice. Moreover, inhibitory synapse structural defects caused by NONO dysfunction were rescued by increasing the number of these receptors in both cells and mice. Thus, despite the broad transcriptional defects caused by NONO deficiency, our experiments highlight this receptor as a player in the etiology of NONO-related synaptic changes. At the moment, it is unknown whether GABAergic deficits might also be a central component of NONO-associated intellectual disability. Favoring such an idea, infusion of GABA$_A$R α2/α3-specific inhibitors (TPA023, L-838417 and NS11394) has shown effects not only on affective behaviors but also on memory and ketamine-induced memory deficits[32,33]. Moreover, disruption of GABA$_A$R α2 oligomerization

leads both to memory deficits and to changes in prepulse inhibition, a phenotype we observed in *Nono*^{gt} mice[34]. Finally, in rats selected for low and high conditioned fear responses, such behavior correlates with levels of $GABA_AR$ α2 expression[35]. However, there is as yet no direct evidence linking the synaptic deficits we describe to the behavioral changes in mutant animals, and so it is unclear whether targeting GABA transmission will have any therapeutic effect in patients.

METHODS

Methods and any associated references are available in the online version of the paper.

Accession codes. Gene Expression Omnibus: GSE62571 and GSE62573.

Note: Any Supplementary Information and Source Data files are available in the online version of the paper.

ACKNOWLEDGMENTS

We are grateful to the patients and their family members for their participation in our study and to the Functional Genomics Center Zürich (FGCZ) for transcriptomic services. This program has received a state subsidy managed by the National Research Agency under the Investments for the Future program bearing the reference ANR-10-IAHU-01.This study was also supported by the Centre National de la Recherche Scientifique (CNRS), the Fondation pour la Recherche Médicale (DEQ20120323702) and the Ministère de la Recherche et de l'Enseignement Supérieur, as well as by the Swiss National Science Foundation, the Zurich Clinical Research Priority Program "Sleep and Health," the Zurich Fonds zur Förderung des akademischen Nachwuchses and the Zurich Neurozentrum (ZNZ). D.M., S.A.B. and S.K.T. are affiliates of the ZNZ Life Sciences Zurich graduate program, and S.A.B. is a member of the Zürich Center for Interdisciplinary Sleep Research (ZIS). The DDD study presents independent research commissioned by the Health Innovation Challenge Fund (grant number HICF-1009-003), a parallel funding partnership between the Wellcome Trust and the UK Department of Health, and the Wellcome Trust Sanger Institute (grant number WT098051). The views expressed in this publication are those of the author(s) and not necessarily those of the Wellcome Trust or the Department of Health. The research team acknowledges the support of the UK National Institute for Health Research, through the Comprehensive Clinical Research Network.

AUTHOR CONTRIBUTIONS

L.C., S.A.B., J.-M.F. and S.K.T. designed the study. J.A., M. Rio and K.P. recruited and evaluated the study subjects. N.B. performed and analyzed the human brain imaging, and D.M., P.S., A.S. and M. Rudin performed and analyzed the mouse brain imaging. M.L. analyzed whole-exome sequencing data and performed transcriptional analysis and western blot analysis on patient cells, and L.G. performed circadian analyses on patient cells. S.M. contributed to whole-exome sequencing data analysis. C.B.-F. performed whole-exome sequencing. N.C. and P.N. performed the bioinformatics studies. R.H. and S.J.M. supplied engineered virus for *in vivo* rescue experiments. D.M. executed and analyzed all experiments on mouse tissues, and D.M. and M.Ž. executed and analyzed experiments in rodent cells. D.M., C.K., F.C., A.-K.F. and D.P.W. performed and analyzed mouse behavioral experiments. A.M. contributed to the clinical evaluation of the patients. K.S.-P. and O.A. contributed to the WES analysis. G.B. prepared cultured neurons for all experiments in this study. All authors contributed to writing and editing the manuscript.

COMPETING FINANCIAL INTERESTS

The authors declare no competing financial interests.

1. Fox, A.H., Bond, C.S. & Lamond, A.I. P54nrb forms a heterodimer with PSP1 that localizes to paraspeckles in an RNA-dependent manner. *Mol. Biol. Cell* **16**, 5304–5315 (2005).
2. Myojin, R. *et al.* Expression and functional significance of mouse paraspeckle protein 1 on spermatogenesis. *Biol. Reprod.* **71**, 926–932 (2004).
3. Shav-Tal, Y. & Zipori, D. PSF and p54^{nrb}/NonO – multi-functional nuclear proteins. *FEBS Lett.* **531**, 109–114 (2002).
4. Dong, X., Sweet, J., Challis, J.R., Brown, T. & Lye, S.J. Transcriptional activity of androgen receptor is modulated by two RNA splicing factors, PSF and p54nrb. *Mol. Cell. Biol.* **27**, 4863–4875 (2007).
5. Amelio, A.L. *et al.* A coactivator trap identifies NONO (p54nrb) as a component of the cAMP-signaling pathway. *Proc. Natl. Acad. Sci. USA* **104**, 20314–20319 (2007).
6. Park, Y., Lee, J.M., Hwang, M.Y., Son, G.H. & Geum, D. NonO binds to the CpG island of oct4 promoter and functions as a transcriptional activator of oct4 gene expression. *Mol. Cells* **35**, 61–69 (2013).
7. Kim, K.K., Kim, Y.C., Adelstein, R.S. & Kawamoto, S. Fox-3 and PSF interact to activate neural cell-specific alternative splicing. *Nucleic Acids Res.* **39**, 3064–3078 (2011).
8. Patton, J.G., Porro, E.B., Galceran, J., Tempst, P. & Nadal-Ginard, B. Cloning and characterization of PSF, a novel pre-mRNA splicing factor. *Genes Dev.* **7**, 393–406 (1993).
9. Kaneko, S., Rozenblatt-Rosen, O., Meyerson, M. & Manley, J.L. The multifunctional protein p54nrb/PSF recruits the exonuclease XRN2 to facilitate pre-mRNA 3′ processing and transcription termination. *Genes Dev.* **21**, 1779–1789 (2007).
10. Kanai, Y., Dohmae, N. & Hirokawa, N. Kinesin transports RNA: isolation and characterization of an RNA-transporting granule. *Neuron* **43**, 513–525 (2004).
11. Izumi, H., McCloskey, A., Shinmyozu, K. & Ohno, M. p54nrb/NonO and PSF promote U snRNA nuclear export by accelerating its export complex assembly. *Nucleic Acids Res.* **42**, 3998–4007 (2014).
12. Nakagawa, S. & Hirose, T. Paraspeckle nuclear bodies—useful uselessness? *Cell. Mol. Life Sci.* **69**, 3027–3036 (2012).
13. Bond, C.S. & Fox, A.H. Paraspeckles: nuclear bodies built on long noncoding RNA. *J. Cell Biol.* **186**, 637–644 (2009).
14. Chen, L.L., DeCerbo, J.N. & Carmichael, G.G. Alu element-mediated gene silencing. *EMBO J.* **27**, 1694–1705 (2008).
15. Prasanth, K.V. *et al.* Regulating gene expression through RNA nuclear retention. *Cell* **123**, 249–263 (2005).
16. Zhang, Z. & Carmichael, G.G. The fate of dsRNA in the nucleus: a p54^{nrb}-containing complex mediates the nuclear retention of promiscuously A-to-I edited RNAs. *Cell* **106**, 465–475 (2001).
17. Brown, S.A. *et al.* PERIOD1-associated proteins modulate the negative limb of the mammalian circadian oscillator. *Science* **308**, 693–696 (2005).
18. Duong, H.A., Robles, M.S., Knutti, D. & Weitz, C.J. A molecular mechanism for circadian clock negative feedback. *Science* **332**, 1436–1439 (2011).
19. Kowalska, E. *et al.* NONO couples the circadian clock to the cell cycle. *Proc. Natl. Acad. Sci. USA* **110**, 1592–1599 (2013).
20. Kowalska, E. *et al.* Distinct roles of DBHS family members in the circadian transcriptional feedback loop. *Mol. Cell. Biol.* **32**, 4585–4594 (2012).
21. de Ligt, J. *et al.* Diagnostic exome sequencing in persons with severe intellectual disability. *N. Engl. J. Med.* **367**, 1921–1929 (2012).
22. Rauch, A. *et al.* Range of genetic mutations associated with severe non-syndromic sporadic intellectual disability: an exome sequencing study. *Lancet* **380**, 1674–1682 (2012).
23. Vissers, L.E., de Vries, B.B. & Veltman, J.A. Genomic microarrays in mental retardation: from copy number variation to gene, from research to diagnosis. *J. Med. Genet.* **47**, 289–297 (2010).
24. Deciphering Developmental Disorders Study. Large-scale discovery of novel genetic causes of developmental disorders. *Nature* **519**, 223–228 (2015).
25. Tyagarajan, S.K. & Fritschy, J.M. Gephyrin: a master regulator of neuronal function? *Nat. Rev. Neurosci.* **15**, 141–156 (2014).
26. Tyagarajan, S.K. *et al.* Regulation of GABAergic synapse formation and plasticity by GSK3β-dependent phosphorylation of gephyrin. *Proc. Natl. Acad. Sci. USA* **108**, 379–384 (2011).
27. Panzanelli, P. *et al.* Distinct mechanisms regulate $GABA_A$ receptor and gephyrin clustering at perisomatic and axo-axonic synapses on CA1 pyramidal cells. *J. Physiol. (Lond.)* **589**, 4959–4980 (2011).
28. Jacob, T.C. *et al.* Gephyrin regulates the cell surface dynamics of synaptic $GABA_A$ receptors. *J. Neurosci.* **25**, 10469–10478 (2005).
29. Mullen, S.A. *et al.* Copy number variants are frequent in genetic generalized epilepsy with intellectual disability. *Neurology* **81**, 1507–1514 (2013).
30. Zhang, G., Neubert, T.A. & Jordan, B.A. RNA binding proteins accumulate at the postsynaptic density with synaptic activity. *J. Neurosci.* **32**, 599–609 (2012).
31. Ruby, N.F. *et al.* Hippocampal-dependent learning requires a functional circadian system. *Proc. Natl. Acad. Sci. USA* **105**, 15593–15598 (2008).
32. Castner, S.A. *et al.* Reversal of ketamine-induced working memory impairments by the $GABA_A$alpha2/3 agonist TPA023. *Biol. Psychiatry* **67**, 998–1001 (2010).
33. Hofmann, M. *et al.* Assessment of the effects of NS11394 and L-838417, alpha2/3 subunit-selective GABA(A) [corrected] receptor-positive allosteric modulators, in tests for pain, anxiety, memory and motor function. *Behav. Pharmacol.* **23**, 790–801 (2012).
34. Hines, R.M. *et al.* Disrupting the clustering of $GABA_A$ receptor α2 subunits in the frontal cortex leads to reduced gamma-power and cognitive deficits. *Proc. Natl. Acad. Sci. USA* **110**, 16628–16633 (2013).
35. Lehner, M. *et al.* Differences in the density of GABA-A receptor alpha-2 subunits and gephyrin in brain structures of rats selected for low and high anxiety in basal and fear-stimulated conditions, in a model of contextual fear conditioning. *Neurobiol. Learn. Mem.* **94**, 499–508 (2010).

ONLINE METHODS

Patients. All human protocols were reviewed and approved by the institutional review board of the Necker Hospital and informed consent was obtained from all subjects involved in this study. The study has UK Research Ethics Committee approval (10/H0305/83, granted by the Cambridge South REC, and GEN/284/12 granted by the Republic of Ireland REC). Written consent was obtained to publish patient photographs.

MCCID1 was the second child of healthy, non-consanguineous parents. Family history is unremarkable. He was born in the 41st week of gestation, after a normal pregnancy and delivery and an Apgar score of 10/10. Parameters at birth were in the normal range (weight 3,370 g, LW 50.5 cm, HC 34 cm). Developmental milestones were delayed: he was able to walk alone at 3 years of age and had limited speech with preserved comprehension. He developed absence seizures at the age of 5 years and continued to have seizures with increased frequency. He had strabismus and myopia. By the age of 15 years, he developed severe kyphoscoliosis. On examination at 17.5 years, his height was 1.79 m (+1 s.d.), his weight 50 kg (−1.5 s.d.) and OFC 60.5 cm (+4 s.d.). Hands and feet were narrow, with long fingers and toes, overriding toes and bilateral ankylosis of the metacarpophalangeal joint of the thumb. He had flat feet with dystrophic nails. He had a long and expressionless face, malar hypoplasia, short palpebral fissures, small and open mouth with drooling, high-arched-palate and enamel defect. He had a slender build and distal amyotrophy. Speech was limited, with simple sentences, severe elocution disability and nasal speech. Extensive metabolic screening was normal. Myotonic dystrophy and fragile X were excluded. Brain MRI demonstrated bilateral megalencephaly, a thick corpus callosum, enlarged white matter, septum pellucidum cyst and a small cerebellum. High resolution cytogenetic studies (array CGH) identified a *de novo* 15q13.3 deletion.

MCCID2, a male, is the first child of healthy, non-consanguineous parents with no medical family history of note. He has three healthy younger sisters (**Fig. 1a**). Because hydramnios and short long bones were noted in the second trimester of pregnancy, amniocentesis was performed and karyotyping showed normal chromosomes, 46,XY. He was born at 37.6 weeks gestation with low birth parameters (weight 2,540 g, BL 46 cm, OFC 35.5 cm) and an Apgar score of 10/10. He presented poor suckling, gastrointestinal reflux, stridor, cryptorchidism and hypotonia from birth. He developed convergent strabismus within the first year of age. Motor skills have been delayed, with head control achieved at 10 months and walking unaided at 3 years of age. At that time language was limited to a few single words. He was of slender build and macrocephalic, with weight and height −2 s.d. and head circumference +2 s.d. His thorax was long and narrow and he developed kyphoscoliosis and pes planus. He was awkward and slow, with weak patellar reflexes. He suffered from drooling, persistent swallowing difficulties and severe elocution disability with nasal speech. He could not blow or smack. He had multiple dental caries due to mouth breathing. Chronic otitis media resulted in conductive hearing loss of 40 to 60 dB and has been treated with grommets. Hands and feet were narrow, with overriding toes and ankylosis of the metacarpophalangeal joint of both thumbs. Although macrocephalic, his forehead was relatively short and narrow with low frontal and temporal hairline. The face was elongated, with upslanting palpebral features, a convergent squint, a thin and high nasal root with deviated nasal septum and large tip with short columella, severe malar hypoplasia, a small open mouth with narrow and high palate, narrow dental arcades and crowding of teeth. Ears were normally placed and folded, with hypoplastic ear lobes. He made constant progress, was toilet trained at about 7 years, speaks in sentences and is able to write his name and read simple words. He has a shy, gentle and cheerful behavior. When last seen at 15 years of age, puberty was delayed and orthopedic surgery for the kyphoscoliosis was planned. Brain MRI performed at 18 months and 8 years showed a thick corpus callosum, asymmetric trigone and lateral ventricles and a Chiari malformation type I (**Fig. 1b**). EEG showed no gross anomaly. Extensive metabolic screening was normal. Skeletal X-rays showed no malformation of the vertebrae. CytoChip (BlueGnome, Cambridge) array-CGH did not detect any copy number variation.

Whole-exome sequencing. Agilent SureSelect libraries were prepared from 3 µg of genomic DNA sheared with a Covaris S2 Ultrasonicator as recommended by the manufacturer. Exome capture was performed with the 50 Mb SureSelect Human All Exon kit (Agilent Technologies) using a multiplex approach with molecular barcodes for traceable identification of samples. Sequencing was carried with the SOLiD5500 (Life Technologies) on a pool of barcoded exome libraries. 75 + 35 paired-end reads were generated and mapped on the human genome reference (NCBI build37/hg19 version) using LifeScope (Life Technologies).

For each subject, sequences produced allowed a mean sequence coverage between 42–87 reads per bp. The average coverage was 70×, with more than 75% of targeted bases covered 15×. Sequence reads were aligned to the human reference genome sequence (assembly GRCh37) using Mapreads. SNPs and indels were called using Genome Analysis Toolkit and Picard Tools. Poorly mapped (less than 3× cover) and low-quality reads (quality score less than 20) were removed. In-house software (PolyWeb) was used to annotate and filter the variants.

Mice. Generation of *Nono*^{gt} mice was described previously[20]. Mice have been backcrossed more than 12 generations to C57/Bl6J. All experiments were performed by comparing adult wild-type and mutant littermates (2–3 months old). Procedures were approved by the veterinary authorities of the Canton of Zürich.

CT and MR scanning and analysis. The skulls of 20 mice per genotype were scanned with *in vivo* 3D micro computed tomography (Quantum Fx, PerkinElmer, Waltham, MA). All mice were sacrificed before scanning and placed in the micro CT in ventral recumbency with the head centered in the field of view. Scans were taken with an isotropic voxel resolution of 59 µm. The protocol used 90 kV and 100 µA with 50 ms per projection, resulting in a total scan time of 3 min for 360°. 3D surface reconstructions of all skulls were created using the Quantum Fx viewer and assessed or scored for signs of deformation and morphological anomalies by two independent investigators. Analysis of skull parameters was done as described previously[36]. Micro MR images were acquired as described previously[37] via high-resolution MRI of the mouse brain at 9.4 T using a cryogenic quadrature transceiver coil (in-plane image resolution 60 × 60 mm^2).

Mouse behavioral experiments. *Statistical models.* Data were analyzed using mixed ANOVA models with genotype (KO, WT) as between-subjects factor. Within-subject factors were added as needed to explore the dependence of genotype effects on place, time or stimulus. Significant interactions and, where necessary, significant main effects were further explored by Tukey-Kramer *post hoc* tests or by splitting the ANOVA model, as appropriate. One-sample *t*-tests were used for follow-up comparisons against chance levels. Variables known to produce strongly skewed distributions and/or frequent outliers were subjected to a log transformation before ANOVA analysis (as indicated, for example, for latency measures). The significance threshold was set at 0.05. The false discovery rate (FDR) control procedure of Hochberg was applied to groups of conceptually related variables within single tests to correct significance thresholds for multiple comparisons.

Prepulse inhibition. The session consisted of a series of six 40-ms startling pulses of different intensities varying between 100 and 120 dB to get an average magnitude of the initial animal's startle response. The animal was then subjected to a succession of six discrete trials. Each trial included a short period of background white noise (control no-stimulus condition), followed by 20-ms prepulses (4, 8, 12, 16 and 20 dB above the background white noise) and 40-ms startling pulses (100 to 120 dB) presented either separately or in combination (prepulse + pulse, with a delay of 100 ms between the two stimuli). The session was completed with six more 40-ms startling pulses and background noise. The time interval between two stimulus presentations varied between 10 and 20 s.

Elevated plus maze. The apparatus was a crossbar-shape maze, comprising two symmetrically arranged open arms equipped with 3-mm ledges and two closed arms equipped with 20-cm walls. The intersection of the four arms formed a small central zone (5 cm × 5 cm). The maze was elevated 38 cm from the ground. The whole apparatus was made of semi-transparent Plexiglas. The mouse was put on the central platform, the head facing a closed arm. The session lasted 5 min, starting once it entered all four paws into one of the arms. The behavioral parameters were recorded online.

Open-field test. The large open-field arena was circular, with a diameter of 150 cm, a white plastic floor and 35-cm-high sidewalls made of white polypropylene. Illumination was by indirect diffuse room light (four 40-W bulbs, 12 lx). Each subject was released near the wall and observed for 10 min. The same procedure was repeated the next day, resulting in a total observation time of 20 min. Movements were tracked using Noldus EthoVision. The number of deposited fecal boli was recorded after each session.

Light-dark box. A 20 × 30 cm lit chamber with transparent Perspex walls (20 cm high) and open top was connected to a 20 × 15 × 20 cm polyvinylchloride box. The box was dark (~10 lx) and completely enclosed, except for the 7.5 × 7.5 cm opening connecting it to the lit chamber. The lit chamber was under direct room light (~450 lx). Each subject was released in the middle of the lit compartment and observed for 5 min. Movements were tracked using Noldus EthoVision. Rearings and grooming were recorded using the keyboard event-recorder provided by the video-tracking system.

Morris water maze. This test was conducted as described previously[38], in ~12-lx light in a 150-cm-diameter water pool. Six trials were conducted per day, each separated by 30–60 min and lasting 2 min: either learning (15 × 15 cm platform 0.5 cm above the water surface) or testing (platform 0.5 cm below water surface). Three days of acquisition and 2 d of reversal training were conducted. Movements were tracked using Noldus Ethovision. Mouse performance was evaluated using Gallagher's measure of proximity (the average distance from the goal during the test) and Whishaw's error (percentage of path outside a 18-cm wide straight corridor connecting release point and goal)[39,40].

Expression analyses. Total cultured human and mouse skin fibroblast RNAs were isolated using the RNeasy Mini Kit (Qiagen). RNA quality was assessed using RNA Nano LabChips and the 2100 Bioanalyzer (Agilent Technologies) and RNA concentration was measured by spectrophotometry (Nanodrop, Thermo Scientific). Briefly, 100 ng of total RNA was reverse transcribed, and second-strand DNA was produced and amplified by *in vitro* transcription in the presence of biotinylated ribonucleotides using the IVT Express kit (Affymetrix). Microarray experiments were performed for two controls and two patients in duplicate on Affymetrix Human PrimeView Arrays (a genome-wide array with 49,293 probe sets) hybridized with fragmented amplified RNA as recommended by the manufacturer. Similarly, mouse RNAs from two *Nono*^{gt} and two wild-type mice were hybridized on Affymetrix GeneChip Mouse Genome 430 2.0 Arrays (a genome wide array allowing the analysis of 39,000 transcripts). Fluorescence data were imported into two analysis software packages: Affymetrix Expression Console and R Bioconductor. Gene expression levels were calculated using the RMA algorithm Expression Console and flags were computed using a custom algorithm in R (http://www.r-project.org/). Assuming that a maximum of 80% of genes are expressed, we selected the 20% lowest values for each microarray to be background expression data measures. We then computed a threshold at 2 s.d. over the mean of the background. All probes whose normalized intensity measures were lower than the computed threshold were flagged 0 instead of 1. The list has been created filtering probes flagged as 1 for at least half of the chips. The group comparisons were done using Student's *t* test. We filtered the resulting *P* values at 5% and used no correction. Cluster analysis was performed by hierarchical clustering using the Spearman correlation similarity measure and average linkage algorithm.

Meta-analysis of human and mouse samples types was performed as previously described[41].

Mouse hippocampal RNAs were extracted using a GenElute Mammalian Total RNA Miniprep Kit (Sigma, St. Louis, MO, USA) according to the manufacturer's instructions. Total RNA was quantified by absorbance spectroscopy and RNA integrity and quality were assessed by 1.0% agarose gel electrophoresis. Total RNA (1 µg) was transcribed to cDNA with SuperScript II (Invitrogen, Carlsbad, CA, USA) using random hexamer primers according to the manufacturer's instructions.

For quantitative real-time PCR (qPCR), we used 20 ng of cDNA, and single transcript levels of genes were detected with the HOT FIREPol EvaGreen qPCR Mix (Solis BioDyne, Tartu, Estonia) and an AB7900 thermocycler. Primers used for detection of synaptic transcripts were as follows: *Actb* (β-actin), AGTGTGACGTTGACATCCGTA (sense), GCCAGAGCAGTAATCTCCTTCT (antisense); *Gphn*, GGCGACCGAGGGAATGAT (sense), CCACCCAACAAA GAAGGATCTT (antisense); *Gabra1*, GGTTGACCGTGAGAGCTGAA (sense), CTACAACCACTGAACGGGCT (antisense); *Gabra2*, CAGTGGCCCATAACA TGACAAT (sense), GGACATTCGGCTTGGACTGT (antisense); *Camk2a*, CCCCTTTCGCCTACATGTGA (sense), GGCTACAGTGGAGCGGCTTA (antisense). Data were analyzed using the comparative CT method[42].

For transcriptome analysis using RNA-seq, the quality of the isolated RNA was determined with a Qubit (1.0) Fluorometer (Life Technologies, California, USA) and a Bioanalyzer 2100 (Agilent, Waldbronn, Germany). RNAs were then processed using the TruSeq Stranded mRNA Sample Prep Kit (Illumina, Inc., California, USA) according to the manufacturer recommendations. The TruSeq SR Cluster Kit v3-cBot-HS or TruSeq PE Cluster Kit v3-cBot-HS (Illumina, Inc., California, USA) was used for cluster generation using 8 pM of pooled normalized libraries on the cBOT. Sequencing was performed on a Illumina HiSeq 2000 system using the TruSeq SBS Kit v3-HS (Illumina, Inc., California, USA) with paired-end 2 × 100 reads or single-end 1 × 100 reads.

RNA-seq reads were quality-checked with fastqc, which computes various quality metrics for the raw reads. Reads were aligned to the genome and transcriptome with TopHat v. 1.3.3. Before mapping, the low-quality ends of the reads were clipped (three bases from the read start and ten bases from the read end). TopHat was run with default options. The fragment length parameter was set to 100 bases with a s.d. of 100 bases. The distribution of the reads across genomic features was assessed on the basis of these alignments. Isoform expression was quantified with the RSEM algorithm[43] with the option for estimation of the read start position distribution turned on.

Cell culture and transfection. Human primary fibroblasts were cultured at 37 °C under 5% CO_2 in RPMI + Glutamax or OPTI-MEM + Glutamax supplemented with 10% FBS and 5% penicillin/streptomycin (complete medium) (Life Technologies).

Mouse primary hippocampal neuron cultures were prepared as described previously[44]. Hippocampal cultures were transfected with 0.5 µg of either eGFP–gephyrin construct or the specific myc–NONO construct according to the protocol described previously[44]. Cells were transfected after 8 DIV and processed for immunofluorescence 7 d later. In cotransfection experiments, the total DNA concentration was maintained at 1.5 µg.

Plasmids used for transfection. The eGFP–gephyrin P1 variant has been described previously[45]. Overexpression of myc-NONO and myc-NONO RRM were conducted using the plasmids described previously[46]. The GABRA2 construct was created amplifying rat cDNA with primers containing HindIII and XhoI sites and subsequent cloning into the pCR3.1 vector.

Western blot. Human primary fibroblasts protein extracts were prepared on ice in lysis buffer (50 mM Tris pH 8, 170 mM NaCl, 0.5% NP-40 X-100, 50 mM NaF and complete EDTA-free protease inhibitor 11697498001, Roche Applied Science). The Bradford protein assay was used to determine the concentration of each sample (B6916-500 Sigma). 20–30 µg of protein extracts were separated by 4–20% SDS-PAGE (SDS-PAGE Mini-Protean TGX Stain Free, no. 4568093, Bio-Rad). Stain-free gels were exposed to UV light for 2.5 min before transfer to 0.2-µm nitrocellulose membranes (Trans-Blot Turbo Transfer Pack, no. 1704158, Bio-Rad). UV-induced fluorescence corresponding to total proteins was first visualized with ChemiDoc MP imaging system, then the membranes were blocked with 5% nonfat dried milk powder (Invitrogen) diluted in PBS-T (PBS with 0.2% Tween-20) for 1–2 h and incubated overnight at 4 °C in 2% milk in PBS-T with the primary antibodies: NONO, SFPQ, PSPC1 and β-actin, the last of these used as a control for protein loading. Membranes were then incubated with horseradish peroxidase–conjugated secondary antibodies. Proteins were visualized using ECL-Plus (GE Healthcare). Various exposure times were performed for either autoradiography films and AGFA development (Curix 60 no. 1829) or Chemidoc system (Bio-Rad). Raw signal intensities were first obtained for target proteins as well as total proteins profile, with the same sample as reference, using volume tools in the ImageLab software (Bio-Rad). Background signal was deducted from each value. Final quantification data were given as a ratio of target signal to total signal.

Mouse brain lysate and sample preparation were performed as described[47]. Each lane was loaded with 50 µg protein and, after blotting, the nitrocellulose membrane was directly blocked for 30 min with a 1% solution of Western Blocking Reagent (Roche Applied Science, Indianapolis, IN, USA).

Antibodies. The following antibodies were used: mouse anti-β-actin (AM4302, 1:20,000; Ambion), rabbit anti-NONO (LS-C31127, 1:2,000; LSBio Cliniscience), rabbit anti-SFPQ (A301-320A, Bethyl), mouse anti-PSPC1 (sc-374181, 1:1,000; Santa Cruz), mouse anti-gephyrin (mAb7a, 1:3,000; or 3B11, 1:10,000; Synaptic Systems, Gottingen, Germany), rabbit anti-vGAT antibody (1:3,000, Synaptic Systems, Gottingen, Germany), guinea pig anti-$GABA_AR$ α2 subunit[17], mouse

doi:10.1038/nn.4169

anti-myc (1:10,000, Roche), rabbit anti-NONO (1:500)[20], rabbit anti-PSPC1 (1:500)[20], rabbit anti-SFPQ (1:500)[20], NeuN (MAB377, Millipore), GFAP (Z0334, DAKO and MAB360, Millipore), PSD-95 (MA1-045, Affinity Bioreagents), β-actin (MAB1501, Millipore). Secondary antibodies were donkey anti-rabbit IgG-HRP antibody (1:20,000; sc-2313, Santa Cruz) or donkey anti-mouse IgG-HRP antibody (1:20,000; sc-2314, Santa Cruz).

Immunocytochemistry and imaging of human skin fibroblasts. Cells were harvested and seeded 1 d before immunocytochemistry experiment with equal cell density for each well. 24 h later, cells were rinsed twice in PBS and fixed in IC fixation buffer (FB001, Invitrogen) for 10 min at room temperature. Cells were then permeabilized with 0.5% Triton X-100 for 10 min at room temperature. After three PBS washes, blocking was done with 5% BSA diluted in 0.1% Triton-PBS for 30 min at room temperature. Hybridization was performed with the first antibodies used in western blotting experiments in a moist chamber overnight at 4 °C. After three 10-min 0.1% Triton-PBS washes, detections were carried out with secondary antibodies Alexa488 anti-rabbit IgG (1:400, A-11034, Life Technologies) and Alexa594 anti-mouse IgG (1:400, A-11005, Life Technologies) for 1 h at room temperature in a dark and moist chamber. After three 10-min 0.1% Triton-PBS washes and a final PBS wash, slides were mounted with ProLong (P36935, Invitrogen). Images were taken with a Zeiss LSM700 microscope fitted with a Plan-Apochromat 40×/1.3 oil DIC M27 objective and Zen 2009 software. Images montage was done using ImageJ.

Immunocytochemistry and immunohistochemistry on mouse samples. Immunocytochemistry was performed as described previously[26]. In short, cells were rinsed in PBS and fixed for 10 min in 4% paraformaldehyde at room temperature. Cells were permeabilized with 0.01% Triton X-100 and detection of intracellular proteins were achieved by incubation for 60 min at room temperature with primary antibodies diluted in PBS containing 10% normal serum, followed by incubation with secondary antibodies coupled to Cy3 or Cy5 (1:500, Jackson ImmunoResearch) for 30 min at room temperature. Finally, coverslips were mounted with fluorescent mounting medium (Dako Cytomation, Carpinteria, CA). The $GABA_AR$ α2 subunit antibody was incubated with living cultures for 90 min in culture medium[48].

Staining and immunohistochemical analysis of synaptic components was performed as previously described. Briefly, mice were anesthetized with pentobarbital and perfused intracardially with ice-cold, oxygenated ACSF. The brain was extracted and cut in blocks containing the regions of interest for analysis (for example, hippocampal formation). The tissue was plunged into ice-cold, freshly prepared fixative (4% PFA in PBS) and postfixed for 90 min, rinsed with PBS, cryoprotected overnight in 30% sucrose in PBS, frozen with powdered dry ice and stored at −80 °C. Sections were cut from frozen blocks with a sliding microtome at a thickness of 40 µm and were collected free-floating in PBS. They were incubated under continuous agitation in primary solution (Tris buffer, pH 7.4, containing 0.2% Triton X-100, 2% normal serum and the primary antibodies) for 15–48 h at 4 °C, washed in Tris buffer and incubated for 30–60 min at room temperature in secondary antibodies coupled to a fluorochrome.

Immunofluorescence images were captured by laser scanning confocal microscopy, using a 20×, 40× or 64× lens (NA 1.4, 1,024 × 1,024 pixels, Zeiss LSM 710). Final illustrations were prepared from the maximal intensity projection of stacks of images spaced at 0.5 µm. Signals were quantified using a custom macro created with ImageJ software. Images were background-subtracted and filtered with a Gaussian filter, but no change in brightness and contrast was applied.

High-resolution *in situ* hybridization. Dissociated hippocampal neurons were prepared and maintained as previously described[49]. *In situ* hybridization was performed using the QuantiGene (QG) ViewRNA kit from Panomics as previously described with the following modifications. Cells (DIV 14) were incubated for 2 min at room temperature in PBS and fixed for 15 min using 4% formaldehyde solution (in PBS, pH 7.4). After fixation, cells were permeabilized using a detergent solution (Panomics) for 5 min. Cells were washed three times with PBS followed by *in situ* hybridization using *Gabra2* and pan-collybistin (*Arhgef9*) probes designed by Panomics, following the manufacturer's instructions. Briefly, probes were diluted 1:100 in hybridization buffer supplied by Panomics, incubated at 40 °C (3 h), washed, hybridized with preamplification oligonucleotides (1:100) at 40 °C (40 min), washed, hybridized with amplification oligonucleotides (1:100) at 40 °C (40 min), washed and, finally, hybridized with label oligonucleotides (1:100) at 40 °C (40 min). Coverslips were dried at room temperature in a vertical position. Coverslips were mounted with Dako-DAPI fluorescent mounting Medium (Dako S3023) and left to polymerize overnight at 4 °C.

Synaptosome preparation. Synaptosomes were prepared as described previously[50]. In brief, mouse brains were homogenized in 5 ml homogenization buffer (0.32 M sucrose, 1 mM EDTA pH 7.4, 1 mM dithiothreitol, phenylmethylsulfonyl fluoride solution (Sigma, 93482-50ML-F), complete mini-protease inhibitor (Roche Diagnostics) for 10 s using a Polytron. The homogenate was centrifuged at 1,000*g* for 10 min at 4 °C, yielding the nuclear fraction and the supernatant. The supernatant was centrifuged at 31,000*g* for 5 min at 4 °C using a discontinuous Percoll gradient. The layer between the 3% and 10% Percoll was collected, washed in 30 ml of homogenization buffer and further centrifuged at 22,000*g* for 15 min at 4 °C. The pellet was resuspended in EBC buffer (50 mM Tris-HCl pH 8.0, 120 mM NaCl and 0.5% NP-40) containing complete mini-protease inhibitor (Roche Diagnostics) and phosphatase inhibitor cocktail 1 and 2 (Sigma-Aldrich) for western blot analysis or lysis buffer for RNA extraction (GenElute Mammalian Total RNA Miniprep Kit, Sigma).

Stereotactic intrahippocampal injections. Adult male mice (8–20 weeks) weighing >25 g were anesthetized with 5% isoflurane in oxygen during head fixation and trepanation; subsequently, isoflurane concentration was reduced to 1.5%. 1 µl of AAV9 encoding pHluorin-tagged GABRA2 (ref. 28) was injected unilaterally into CA3 of the hippocampus under stereotaxic guidance (coordinates from bregma: antero-posterior −2.0 mm; medio-lateral 2.3 mm; dorso-ventral 2.4 mm from the skull). During the operation and recovery, mice were held on a warm pad. For recovery, the mice were housed singly until behavior returned to normal.

36. Yang, B. *et al.* Sh3pxd2b mice are a model for craniofacial dysmorphology and otitis media. *PLoS ONE* **6**, e22622 (2011).
37. Baltes, C., Radzwill, N., Bosshard, S., Marek, D. & Rudin, M. Micro MRI of the mouse brain using a novel 400 MHz cryogenic quadrature RF probe. *NMR Biomed.* **22**, 834–842 (2009).
38. Mohajeri, M.H. *et al.* Intact spatial memory in mice with seizure-induced partial loss of hippocampal pyramidal neurons. *Neurobiol. Dis.* **12**, 174–181 (2003).
39. Gallagher, M., Burwell, R. & Burchinal, M. Severity of spatial learning impairment in aging: development of a learning index for performance in the Morris water maze. *Behav. Neurosci.* **107**, 618–626 (1993).
40. Whishaw, I.Q. Cholinergic receptor blockade in the rat impairs locale but not taxon strategies for place navigation in a swimming pool. *Behav. Neurosci.* **99**, 979–1005 (1985).
41. Cros, J. *et al.* Human $CD14^{dim}$ monocytes patrol and sense nucleic acids and viruses via TLR7 and TLR8 receptors. *Immunity* **33**, 375–386 (2010).
42. Schmittgen, T.D. & Livak, K.J. Analyzing real-time PCR data by the comparative C(T) method. *Nat. Protoc.* **3**, 1101–1108 (2008).
43. Li, B. & Dewey, C.N. RSEM: accurate transcript quantification from RNA-Seq data with or without a reference genome. *BMC Bioinformatics* **12**, 323 (2011).
44. Buerli, T. *et al.* Efficient transfection of DNA or shRNA vectors into neurons using magnetofection. *Nat. Protoc.* **2**, 3090–3101 (2007).
45. Lardi-Studler, B. *et al.* Vertebrate-specific sequences in the gephyrin E-domain regulate cytosolic aggregation and postsynaptic clustering. *J. Cell Sci.* **120**, 1371–1382 (2007).
46. Kuwahara, S. *et al.* PSPC1, NONO, and SFPQ are expressed in mouse Sertoli cells and may function as coregulators of androgen receptor-mediated transcription. *Biol. Reprod.* **75**, 352–359 (2006).
47. Fritschy, J.M. & Mohler, H. $GABA_A$-receptor heterogeneity in the adult rat brain: differential regional and cellular distribution of seven major subunits. *J. Comp. Neurol.* **359**, 154–194 (1995).
48. Brunig, I., Suter, A., Knuesel, I., Luscher, B. & Fritschy, J.M. GABAergic terminals are required for postsynaptic clustering of dystrophin but not of $GABA_A$ receptors and gephyrin. *J. Neurosci.* **22**, 4805–4813 (2002).
49. Notter, T., Panzanelli, P., Pfister, S., Mircsof, D. & Fritschy, J.M. A protocol for concurrent high-quality immunohistochemical and biochemical analyses in adult mouse central nervous system. *Eur. J. Neurosci.* **39**, 165–175 (2014).
50. Dunkley, P.R., Jarvie, P.E. & Robinson, P.J. A rapid Percoll gradient procedure for preparation of synaptosomes. *Nat. Protoc.* **3**, 1718–1728 (2008).